MNRAS **000**, 1–13 (2021) Preprint 5 August 2021 Compiled using MNRAS LaTeX style file v3.0

Filling the gap between synchronized and non-synchronized sdBs in short-period sdBV+dM binaries with TESS: TIC 137608661, a new system with a well defined rotational splitting

Roberto Silvotti,[1⋆] Andrzej S. Baran,[2,3,4] Péter Németh,[5] John H. Telting,[6]
Roy H. Østensen,[3] Jakub Ostrowski,[2] Sumanta K. Sahoo[2,7]

[1] *INAF-Osservatorio Astrofisico di Torino, Strada dell'Osservatorio 20, 10025 Pino Torinese, Italy*
[2] *ARDASTELLA Research Group, Institute of Physics, Pedagogical University of Krakow, ul. Podchorążych 2, 30-084 Kraków, Poland*
[3] *Department of Physics, Astronomy and Materials Science, Missouri State University, 901 S. National, Springfield, MO 65897, USA*
[4] *Embry-Riddle Aeronautical University, Department of Physical Science, Daytona Beach, FL 32114, USA*
[5] *Astronomical Institute of the Czech Academy of Sciences, CZ-251 65, Ondřejov, Czech Republic*
[6] *Astroserver.org, Fő tér 1, 8533 Malomsok, Hungary*
[7] *Nicolaus Copernicus Astronomical Centre of the Polish Academy of Sciences, ul. Bartycka 18, 00-716 Warsaw, Poland*

Accepted XXX. Received YYY; in original form ZZZ

ABSTRACT

TIC 137608661 is a new sdBV+dM binary system discovered by the *TESS* space mission with an orbital period of 7.21 hours. Once removed the orbital frequency and its harmonics, the Fourier transform of TIC 137608661 shows a rich spectrum of g-mode pulsation frequencies from the sdB star. The amplitude spectrum is particularly simple to interpret as we immediately see several rotational triplets of equally spaced frequencies. The central frequencies of these triplets are equally spaced in period with a mean period spacing of 270.12 s, corresponding to consecutive l=1 modes. From the mean frequency spacing of 1.25 μHz, we derive a rotation period for the sdB star of 4.6 days, significantly longer than the orbital period. Among the handful of sdB+dM binaries for which the sdB rotation was measured through asteroseismology, TIC 137608661 is the non-synchronized system with both the shortest orbital period and the shortest sdB rotation period. Only NY Vir has a shorter orbital period but it is synchronized. This article contains also the results of a spectroscopic follow-up that allows us to measure the radial velocities of the sdB star and to determine its main atmospheric parameters. Moreover, an analysis of the spectral energy distribution of TIC 137608661, together with a comparison between sdB pulsation properties and asteroseismic models, gives us further elements to constrain the system.

Key words: stars: horizontal branch; stars: binaries; stars: oscillations (including pulsations); asteroseismology; stars: individual: TIC 137608661.

1 INTRODUCTION

Hot subdwarf B (sdB) stars are core-helium burning stars which have had their hydrogen-rich envelopes stripped almost completely during the red giant phase, most likely as a result of binary interaction (Han et al. 2002, 2003; Clausen et al. 2012; Pelisoli et al. 2020).

Among hot subdwarfs (a class of stars that includes sdB and sdO stars, see Heber 2016 for a recent review), ∼30% are in wide binaries with F/G/K companions, while ∼35% are apparently single (see e.g. Silvotti et al. 2021, and references therein). A handful of single sdBV (= sdB Variable, i.e. pulsating) stars, for which rotation was accurately measured through asteroseismology, show typical rotation periods between ∼30 and ∼100 days (Charpinet et al. 2018; Reed et al. 2018a, and references therein).

The remaing fraction of hot subdwarfs (∼35%) are in post-common-envelope short-period binaries with M-dwarf or white dwarf (WD) companions. For this subclass of systems, the rotation periods from asteroseismology appear to

---

[⋆] E-mail: roberto.silvotti@inaf.it

be shorter as the orbital period decreases (Charpinet et al. 2018). But only in three systems, HD 265435, NY Vir and KL UMa, with orbital periods of only 1.65, 2.42 and 8.25 hours respectively, the sdBV primary is fully synchronized (Pelisoli et al. 2021; Charpinet et al. 2008; Van Grootel et al. 2008), at least in the outer layers of the star. At orbital periods shorter than 8 hours, a dozen of systems fully synchronized or very close to synchronization was found with a different technique, with the sdB/sdO rotation velocity measured from the spectral line broadening (references are given in the caption of Figure 15).

Theoretical calculations of tidal synchronization timescales fail to account for the synchronization of sdB stars (Preece et al. 2018) and not even a larger convective core is able to explain the synchronization of NY Vir (Preece et al. 2019). Following these authors, the synchronization of NY Vir could be explained either by a partial synchronization of at least the outer layers of the star already during the common envelope phase, or by higher convective mixing velocities respect to those obtained with the mixing lenght theory.

The binary system described in this paper, TIC 137608661 (alias TYC 4544-2658-1 or FBS 0938+788), is a new bright sdBV+dM binary (Gaia EDR3 magnitude G = 11.112±0.001), located at ∼256 pc from us (Gaia EDR3 parallax of 3.90±0.04 mas). This star was "not observed to vary" in a short time-series photometry run of about 10 minutes at the Nordic Telescope, with a sampling time of 8 seconds, excluding short-period p-modes with amplitudes higher than about 1 ppt (part per thousand, Østensen et al. 2010). In the next sections we present the results of an analysis of the *TESS* light curve of TIC 137608661. The orbital characteristics are described in section 2, together with the results of a spectroscopic follow-up that allows us to measure the radial velocities of the sdB star, to determine its $T_{\rm eff}$, $\log g$ and chemical abundances, and to constrain the binary system, using also an analysis of the spectral energy distribution. In section 3 a detailed analysis of the pulsational spectrum of the sdB star is given, and the characteristics of the sdB star obtained from spectroscopy are compared with those obtained from evolutionary pulsation models. In section 4 the rotation period of TIC 137608661, derived from asteroseismology, is compared with other similar sdBs in short-period binaries that are or are not synchronized with their orbital period.

2 CONSTRAINING THE BINARY SYSTEM

2.1 *TESS* light curve and ephemeris

TIC 137608661 was observed by the *TESS* space telescope during sector 14, 20 and 26, each sector being ∼27 days long, with a sampling time of 2 minutes. We downloaded the data from the *TESS* Asteroseismic Science Operations Center (TASOC)[1] and we used the PDCSAP fluxes (PDC=Presearch Data Conditioning, SAP=Simple Aperture Photometry, see *TESS* documentation for more details). After having removed some outliers and some short subsets near the sector edges for which an instrumental trend was clearly present, the data we used consists of three sets with a length of 26.47, 26.32 and 24.84 days respectively, corresponding to the following dates in ($\rm BJD_{\it TBD}$−2457000): 1683.7-1710.2 (19/07/2019-14/08/2019), 1842.5-1868.8 (25/12/2019-20/01/2020), and 2010.3-2035.1 (09/06/2020-04/07/2020). When considering all three sectors together, the frequency resolution (1.5/T, where T is the total length) is about 0.049 μHz.

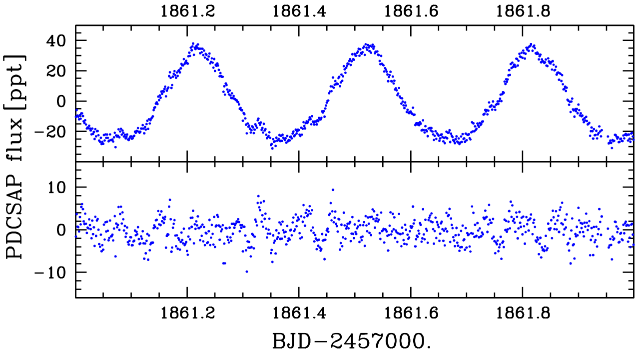

Figure 1. A representative 1-day section of the *TESS* light curve. Top: original data. Bottom: residuals after removing the orbital frequency and its harmonics.

A representative 1-day section of the light curve is shown in Figure 1. We see that the light curve is dominated by a strong regular modulation with a period of 7.21 hours and a relative amplitude of 2.88%, typical of a reflection effect by a cooler companion. Moreover, when we subtract the orbital modulation (lower panel of Figure 1), we see residual low-amplitude variations suggesting that the sdB component is a pulsating star.

The *TESS* data were firstly used to compute the ephemeris of the system. The following equation gives the times of the photometric maxima, when the cool companion is behind the sdB star and shows its heated hemisphere (corresponding to phase 0.5 in Figure 2). $\rm BJD_{\it TDB}$ 2458683.970519 is the time of the first maximum in the *TESS* data.

$$\begin{aligned}\rm BJD_{\it TDB} = & (2458683.970519 \pm 0.000035)+ \\ & (0.300420467 \pm 0.000000086)\,\rm E\end{aligned}$$

2.2 Spectroscopy

Thirteen low-resolution spectra of TIC 137608661 were obtained at the Nordic Optical Telescope (NOT, La Palma) using ALFOSC, 250 s exposure times, grism#18, 0.5 arcsec slit, and CCD#14, giving an approximate wavelength range 345-535 nm. The spectra were homogeneously reduced and analysed. Standard reduction steps within IRAF include bias subtraction, removal of pixel-to-pixel sensitivity variations, optimal spectral extraction, and wavelength calibration based on helium arc-lamp spectra. The peak signal-to-noise ratio of the individual spectra ranges from 80 to 250. The spectra were taken at different orbital phases and the radial velocities (RVs) were measured using the lines Hβ, Hγ, Hδ, H8 and H9 through a cross-correlation analysis in which we used as a template a synthetic fit to an orbit-corrected average (all spectra were shifted to zero velocity

---

[1] https://tasoc.dk/

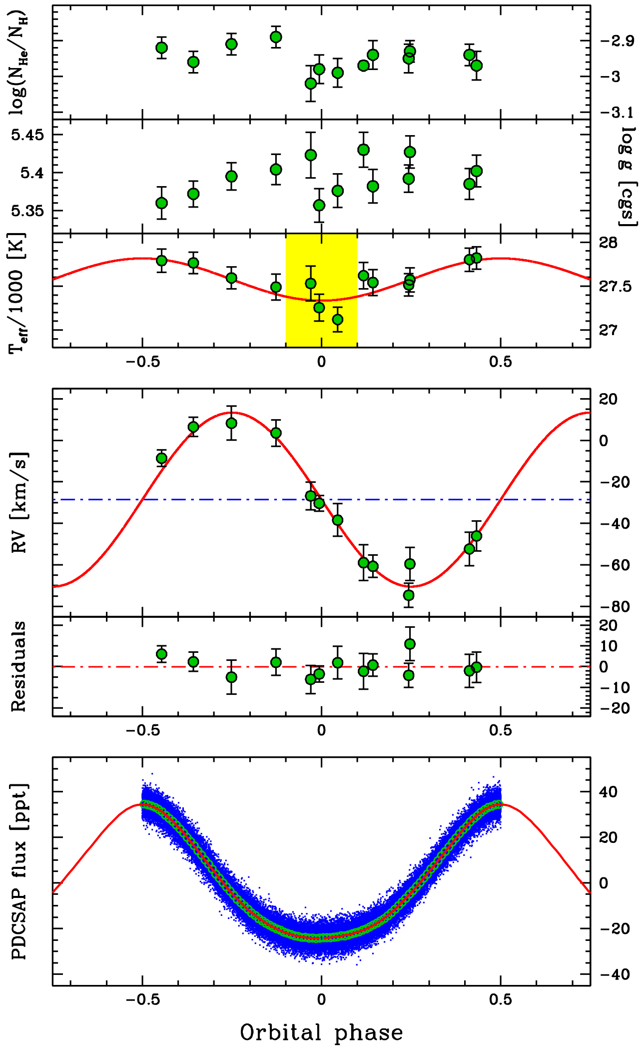

Figure 2. Phase resolved spectroscopy vs photometry of TIC 137608661. Upper panels: He abundance, $\log g$ and $T_{\rm eff}$ as a function of the orbital phase. $T_{\rm eff}$ shows a clear orbital modulation due to the contribution of the M-dwarf companion and for this reason we assume as best $T_{\rm eff}$ the mean of the three measurements in the phase range –0.1 - 0.1 (yellow rectangle), when the contribution of the secondary star is minimum. Middle panels: radial velocities of the sdB star and residuals. Lower panel: single *TESS* data (blue dots), mean data in 100 phase bin (green open dots) and best fit (red). Note that the orbital modulation is not perfectly sinusoidal and indeed the fit was performed using also the threee harmonics listed in Table 2. Like in other sdB+dM systems, this behaviour may depend on the values of the various parameters that describe the so-called reflection effect (see e.g. Budaj 2011 for a detailed approach).

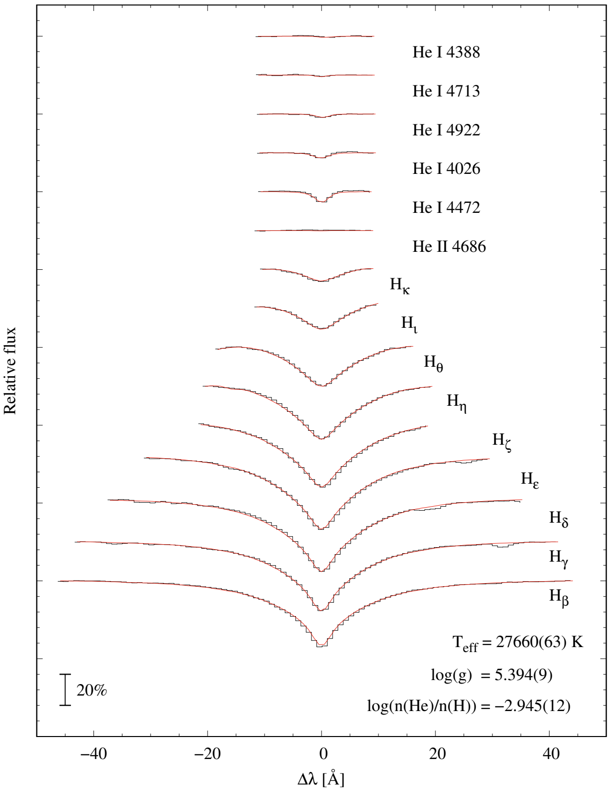

Figure 3. LTE fit to the mean orbit-corrected spectrum obtained from all the thirteen ALFOSC spectra.

before averaging). Since the RVs obtained from the last six spectra, all taken on the same night, showed a positive offset respect to the previous measurements, we applied to them a correction of –19.3 km/s. This number was obtained by minimizing the residuals of the least squares fit. We obtain a RV amplitude K=41.9±1.3 km/s and a system velocity V=–28.6±1.2 km/s.[2]

After determining the orbital RV amplitude, we shifted the spectra to the system frame of rest, and computed a mean spectrum using all the thirteen spectra. The mean spectrum reaches a peak S/N of ∼540 in the region 4725 – 4785Å. We then used this mean spectrum to determine the physical parameters of the target through spectroscopic model fitting.

We first did a fit using the same H/He LTE grid of Heber et al. (2000) for consistency with earlier studies. We used all the Balmer lines from $H\beta$ to $H\kappa$, as well as the five strongest He I lines for the fit. The LTE fit resulted in values of $T_{\rm eff} = 27660 \pm 64$ K, $\log g = 5.394 \pm 0.009$, $\log(N_{\rm He}/N_{\rm H}) = -2.945 \pm 0.012$. The errors listed on the measurements are the formal errors of the fit, which reflect only the signal-to-noise ratio of the mean, and not any systematic effects caused by the assumptions underlying those models. The best fit of the mean spectrum is shown in Figure 3.

Then, as a next step, we performed a fit of each individual spectrum in order to measure the variations of the atmospheric parameters as a function of the orbital phase, which are shown in Figure 2, together with RVs and *TESS* photometric data. Since $T_{\rm eff}$ shows a clear orbital modulation due to the contribution of the M-dwarf companion, we assume as best $T_{\rm eff}$ the mean of the three measurements near

---

[2] Without applying any correction to the last six RVs, the RV amplitude does not change significantly (we obtain 44.1±3.7 km/s), while the system velocity is reduced to –20.0±2.9 km/s.

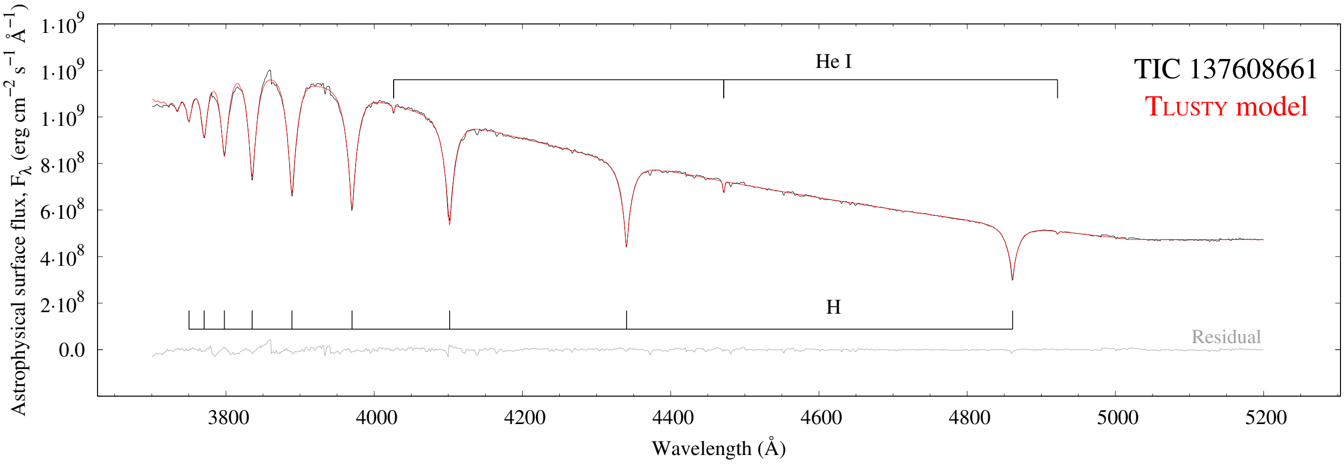

Figure 4. Best-fitting Tlusty/XTgrid non-LTE model (red) to the mean orbit-corrected spectrum obtained from all the thirteen ALFOSC spectra (black). The observed spectrum has been adjusted to the continuum of the final theoretical model. **NOT THE FINAL VERSION!**

phase 0, when the secondary star stands in front of the sdB primary and its contribution is minimum. Instead, for $\log g$ and $\log(N_{\rm He}/N_{\rm H})$, we use the mean of all 13 measurements. Our best values for the sdB atmospheric parameters are: $T_{\rm eff}$=27300±200 K, $\log g$=5.39±0.04, $\log(N_{\rm He}/N_{\rm H})$=−2.95±0.05.

To determine the atmospheric parameters of TIC 137608661 in non-Local Thermodynamic Equilibrium (non-LTE), we fitted the co-added ALFOSC observations with synthetic spectra calculated from Tlusty models (v207; Hubeny & Lanz 2017; Lanz & Hubeny 2007). The models include opacities from H, He, C, N, O, Ne, Mg, Si, and Fe. The spectral analysis was done with a steepest-descent spectral analysis procedure, implemented in the XTgrid code (Németh et al. 2012). XTgrid calculates new model atmospheres and corresponding synthetic spectra iteratively in the direction of decreasing chi-squares. The synthetic spectra are normalized in 80 Å sections to the observation to reduce the effects of the uncalibrated continuum flux on the parameter inference. Figure 4 shows the best-fit non-LTE model to the mean ALFOSC spectrum. The convergence of the fit is obtained when the relative changes of all model parameters decrease below 0.5%. Next, error calculations are performed by mapping the chi-square surface around the best fit. For abundances, the error bars are evaluated in one dimension, and parameter correlations are included for $T_{\rm eff}$ and $\log g$ as in Figure 5.

The spectroscopic parameters obtained from LTE and non-LTE models are summarized in Table 1.

2.3 Spectral Energy Distribution

Spectral energy distributions (SED) provide a way to evaluate the contributions of binary members to the observed flux. Hot subdwarf stars with F- or G-type companions can be described with two components, which contribute nearly equally to the observed flux in the optical. Late K- and M-type companions remain nearly invisible next to a hot subdwarf. The only exceptions are those in close orbits, when the irradiation by the hot subdwarf is able to form a hot spot on the companion. The strength of irradiation depends on

Table 1. Spectroscopic parameters from LTE and non-LTE models.

Parameter	LTE	non-LTE
$T_{\rm eff}$ (K)	27300 ± 200	27960 ± 50
$\log g$ (cm s^{-2})	5.39 ± 0.04	5.42 ± 0.04
$\log n{\rm He}/n{\rm H}$	-2.95 ± 0.05	-2.89 ± 0.05
$\log n{\rm C}/n{\rm H}$		-5.68 ± 0.25
$\log n{\rm N}/n{\rm H}$		-4.53 ± 0.16
$\log n{\rm O}/n{\rm H}$		-4.36 ± 0.03
$\log n{\rm Ne}/n{\rm H}$		< -3.6
$\log n{\rm Mg}/n{\rm H}$		-4.83 ± 0.17
$\log n{\rm Si}/n{\rm H}$		-5.93 ± 0.15
$\log n{\rm Fe}/n{\rm H}$		-4.73 ± 0.22

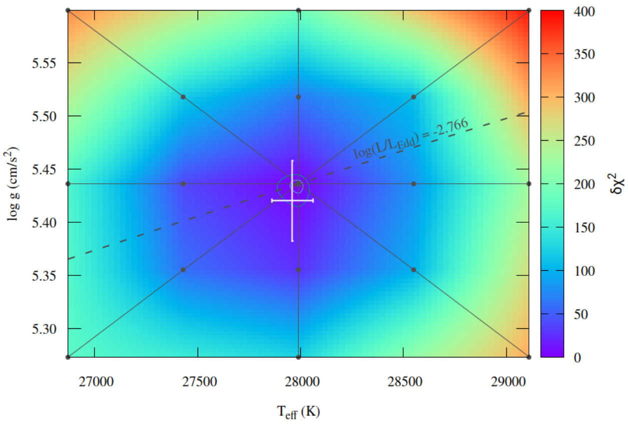

Figure 5. Non-LTE $T_{\rm eff} - \log g$ correlation and two dimensional error determination for TIC 137608661. The color bar shows the chi-square variations with the parameters. The contours are for 60, 90 and 99% confidence intervals.

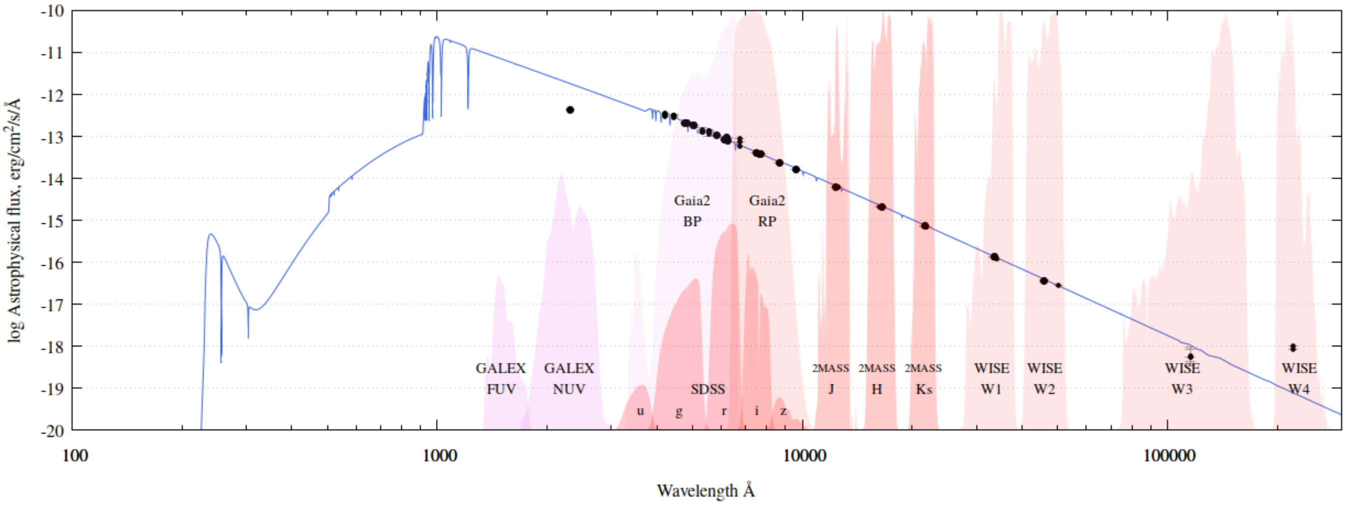

Figure 6. The spectral energy distribution of TIC 137608661. All data points were taken from the VizieR photometric data service. The shaded regions mark various filter pass-bands. The SED shows that the GALEX NUV flux measurement is off, while all other measurements can be modeled consistently with a single stellar component. **ASB: WISE W4 is also off. Any comments needed?**

the radii of the components, their separation, as well as the temperature and the spectral properties of the irradiating star. In TIC 137608661 the amplitude of the reflection effect is relatively low, only ∼6% (57.5 ppt) when we consider the total amplitude, i.e. the difference between maximum and minimum flux. In HW Vir and NY Vir this contribution is about 20% in the optical, but a precise spectral characterization of the cool companion is still difficult, while in the sdO+dM binary AA Dor it was possible (Vučković et al. 2016) despite the reflection effect amplitude is only ∼7%.

For a SED analysis XTGrid collects photometric data from the VizieR Photometry Viewer[3] around 2 arcseconds of the target and shifts the synthetic SED calculated from the spectral modeling to the photometric data. The interstellar extinction toward TIC 137608661 is low, $E(B-V) = 0.017$ mag (Schlafly & Finkbeiner 2011). Figure 6 shows that the match over the optical and infrared regions is excellent and the SED can be modeled with a single hot component. However, a cool ($T_{\rm eff} \lesssim 4000$ K) M dwarf can remain invisible in the SED. The ultraviolet region is very important because the SED of the subdwarf peaks there. Unfortunately, the only measurement from GALEX is significantly off, most likely due to the bright non-linearity of the GALEX photometry (Morrissey et al. 2007). Based on the optical spectrum, the ultraviolet flux must be much higher.

With an independent distance measurement provided, the SED analysis returns the mass, radius and luminosity of the hot subdwarf. We used the Gaia EDR3 distance of $d =$ 256.5±2.6 pc and found $M = 0.44{\pm}0.02$ M$_\odot$, $R = 0.21{\pm}0.05$ R$_\odot$ and $L = 24.5 \pm 1.0$ L$_\odot$ for the sdB in TIC 137308661.

Following Deca et al. (2012), the B–V=–0.37 and J–Ks=–0.187 mag color indices suggest a very low contribution from the companion. Maxted et al. (2002) have derived a relationship between the separation and relative radii of the components that can be used to estimate the amplitude of the reflection effect for different companion types. At a similar orbit a white dwarf would produce a reflection amplitude 100 times less than a cool main sequence star. This factor is large enough, that even at an orbital inclination as low as 40°, the observed amplitude rules out a white dwarf companion. Further spectral characterization of the companion would require very high SNR infrared spectroscopy.

3 SDB PULSATIONS

3.1 Fourier analysis

The Fourier transform of the *TESS* data in Figure 7 shows a rich spectrum. The low-frequencies are dominated by the orbital modulation at 38.526 μHz plus its harmonics at 77.052, 115.578 and 154.105 μHz. As expected, these harmonics have decreasing amplitudes: 4.74, 0.42 and 0.26 ppt respectively. A fourth harmonic at 192.645 μHz has an amplitude of 0.27 ppt, higher than expected, and indeed, as we will see, this frequency is also part of a triplet of pulsation frequencies, suggesting that a tidal-induced mechanism might be at work in this case. At frequencies higher than 90 μHz, up to ∼370 μHz, many peaks with amplitudes of several hundreds of ppm (part per million) correspond to a typical sdB spectrum of g-mode pulsations. A few lower-amplitude peaks (∼100 ppm) are present also at higher frequencies, up to 690 μHz.

To define a reliable noise threshold we proceeded as follows. First we computed the signal-to-noise ratio (S/N) corresponding to a False Alarm Probability (FAP) of 0.1% following Kepler (1993): S/N=ln(n$_f$*1000)$^{0.5}$ in which n$_f$=F$_N$/R$_f$ is the number of independent frequencies, F$_N$ is the Nyquist frequency, R$_f$=1/ΔT is the nominal frequency resolution and ΔT is the total duration of the run. We obtain S/N=4.5. Then, to test the reliability of this number, we computed the FT of 1000 simulated light curves obtained by reshuffling in a random way the data, after having removed 57 significant peaks (those in Table 2). Since reshuffling destroys any coherent signal, the S/N ratio of the highest peak of each FT was used to test the previous S/N expression. We found that the expression is valid as long as an offset

---

[3] `http://vizier.u-strasbg.fr/vizier/sed/`

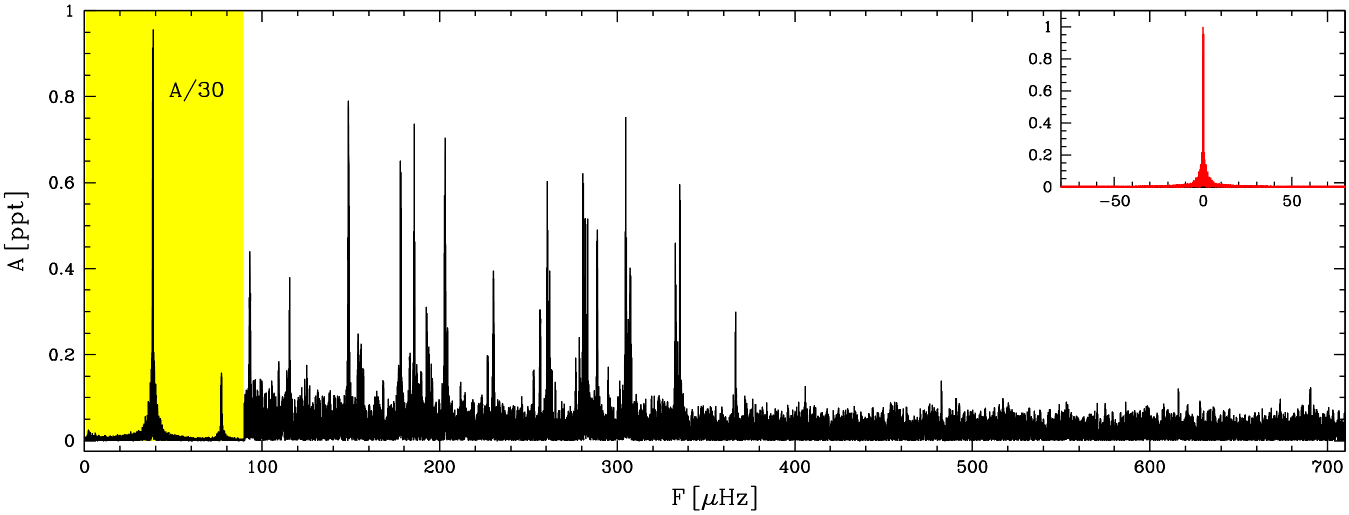

Figure 7. Amplitude spectrum of TIC 137608661 using all three sectors together. The yellow section corresponds to the orbital frequency and its first harmonic. The upper-right inset is the window function (in red).

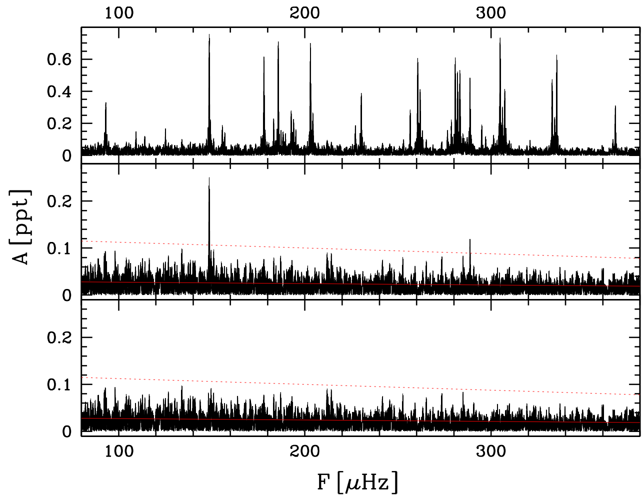

Figure 8. Prewhitening procedure. Upper panel: spectrum of TIC 137608661 in the main pulsation region. Central panel: residuals after having removed 55 significant peaks. Bottom panel: residuals after having removed also f6b and f33b. The solid red line and the dotted red line are the mean noise level and the detection threshold, respectively. See text for more details.

is used and this offset is independent from the number of simulations suggesting that it is robust. For this data set the offset on S/N is +0.5 or +0.8 depending whether we use the FT mean noise or the FT median noise as the denominator. These numbers are very similar to those found by Baran & Koen (2021) in their simulations. In conclusion, using the FT mean noise, we adopted S/N=5.0 as our threshold for real pulsation frequencies, while the peaks with 4.5<S/N<5.0 are considered as candidates only. Once the signal-to-noise threshold has been set, we must consider that the mean noise is not constant everywhere. Since it is flat at high frequencies but tends to increase at low frequencies (due to low-amplitude peaks, below the threshold, unresolved peaks, aliasing effects, etc., which are not removed by prewhitening), after some measurements in different frequency intervals we decided to adopt a noise model which is linearly decreasing between 90 and 380 μHz (0.027 ppt at 90 μHz and 0.019 ppt at 380 μHz) and remains constant at 0.019 ppt up to 700 μHz.

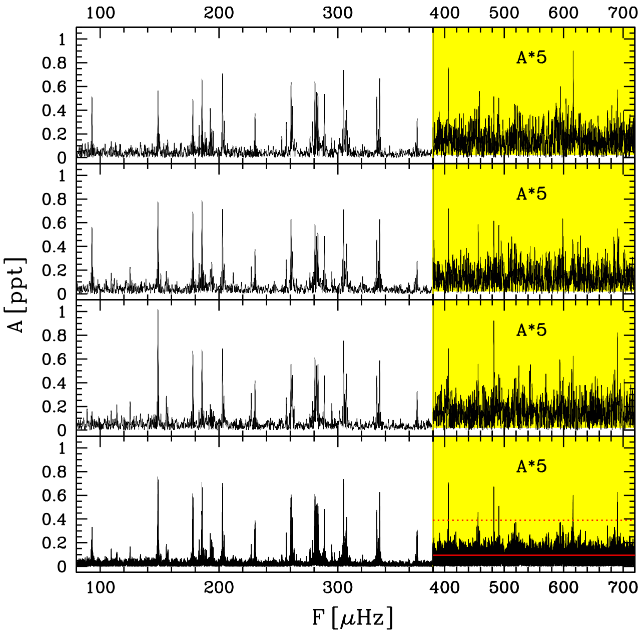

Figure 9. Amplitude spectrum of each single sector. From top to bottom: sector 14, 20, 26 and all three sectors together. Like in Figure 8, the solid red line and the dotted red line are the mean noise level and the detection threshold, respectively.

We applied to the light curve a standard prewhitening procedure with nonlinear least-squares fitting and obtained a list of frequencies that is shown in Table 2. Those with S/N between 4.5 and 5.0, that are considered as candidates only, are marked with parentheses in Table 2. The prewhitening procedure is illustrated in Figure 8. After prewhitening, only two frequencies were not completely removed from the amplitude spectrum (central panel of Figure 8), leaving residuals that could be due either to pairs of very close frequencies below the frequency resolution, or to frequency instability (frequencies and/or amplitudes that vary over time).

When we compare the amplitude spectra of the various sectors (Figure 9), we see that most peaks are rather stable in amplitude.

3.2 Period spacing, frequency splitting, inclination of the rotation axis

Looking at the amplitude spectrum of TIC 137608661, we immediately note four consecutive triplets of equally spaced frequencies between ∼260 and ∼340 μHz with a frequency spacing of about 1.3 μHz (Figure 10 upper panel). Another triplet located near ∼190 μHz and a few doublets between ∼150 and ∼370 μHz show a very similar frequency spacing. When we plot the same region of the spectrum in the period domain (lower panel of Figure 10), we see that the central peaks of the four well defined triplets between 260 and 340 μHz are equally spaced in period. The period difference between the central peaks at 3818.7, 3546.0, 3266.9 and 2993.6 s is 272.7, 279.1 and 273.3 s respectively, confirming that the triplets are consecutive l=1 modes. The mean period spacing of these four triplets is 275.03 s. Since the central peak of the triplet near ∼190 μHz, which has a period of 5156.9 s, is also well compatible with the l=1 sequence of modes, we include also this period in the computation of the mean period spacing. From a linear least-squares fit to the five m=0 periods we obtain ΔP= 270.12 ± 1.19 s. Using this value, several other doublets fall close to the expected periods (assuming a perfectly constant spacing) and therefore we adopt 270.12 s in our analysis. Once the period spacing is fixed, we were able to identify further modes, including a few l=1 single peaks at short and long periods. The geometry of the identified modes (number of radial nodes n, spherical degree l, and azimuthal quantum number m) is reported in Table 2. In Figure 11 the "échelle diagramme" of the l=1 sequence shows the residuals between the observed and the theoretical periods. We note the typical meandering shape between ∼2000 and ∼5000-6000 s that is also seen in other sdB pulsators such as KIC 10553698A (Østensen et al. 2014b), EPIC 211779126 (Baran et al. 2017), KIC 10001893 (Uzundag et al. 2017), KIC 11558725 (Kern et al. 2018), PHL 457 (Baran et al. 2019). And we see that the periods at n=22 (f9) and n=25 (f7 and f8) are significantly shorter than the expected values from a constant period spacing, indicating a possible mode trapping. Although an incorrect identification as dipole modes can not be totally excluded, the frequency difference between f7 and f8, equal to 1.29 μHz, suggests that f7 and f8 are indeed two components of the same l=1 triplet.

Figure 12 shows all the complete or incomplete l=1 triplets of frequencies split by the rotation of the star. Considering all of them, we obtain a mean frequency splitting of 1.254 μHz corresponding to a stellar rotation period of about 4.6 days.

The rotation period is obtained from the expression $\mathrm{P_{rot}}=(1-\mathrm{C}_{nl})/\delta\sigma_{nl}$ (where $\delta\sigma_{nl}$ is the frequency spacing), which is valid for a slowly rotating star with $\Omega_{\rm rot} << \sigma_{\rm puls}$. For high-order g-modes, in the asymptotic limit, we can use the following approximation: $\mathrm{C}_{n,l} \simeq 1/[(l\,(l{+}1)]$ and we obtain $\mathrm{C}_{(l=1)}{\simeq}1/2$ and $\mathrm{C}_{(l=2)}{\simeq}1/6$ (Ledoux 1951; Unno et al. 1989; Aerts et al. 2010). Although a sequence of l=2 equally spaced periods is not seen in our data, from the l=1 splitting of 1.254 μHz we can compute the expected frequency splitting for the l=2 modes: $\delta\sigma_{(l=2)} \simeq \frac{5}{3}\,\delta\sigma_{(l=1)}{\simeq}\,2.090$ μHz. And indeed we see two multiplets of frequencies (a doublet and a triplet) which have frequency separations very close to this number. These incomplete quintuplets are shown in the lower panels of Figure 12 and are reported in Table 2. The l=2 spherical degree has been tentatively attributed also to a few other frequencies.

There is another valuable piece of information that can be derived from the very clean amplitude spectrum of TIC 137608661. Having a certain number of clearly identified l=1 triplets, we can analyze the amplitude of each m-component to derive an estimate of the inclination of the rotation axis respect to the line of sigh. More precisely, the geometric visibility of each m-component, and therefore its amplitude, depends on the angle between the pulsation axis and the line of sigh. However, misalignements between pulsation and rotation axis, which would split each l=1 mode in nine components (Pesnell 1985), have never been seen in sdB stars. Thus we can safely assume that pulsation and rotation axes are aligned. If we also assume that, on average, each m-component of a multiplet receive the same amount of energy and develop approximately the same intrinsic amplitude level, then the mean amplitude ratio between m=±1 and m=0 components of a certain number of triplets should directly reflect the inclination of the rotation axis. With five well-defined triplets, this measurement should already have some level of accuracy. In Figure 13 we show the relative amplitudes of the components of the five triplets, the mean amplitudes of the m=–1,0,+1 components, and their errors. A comparison of these numbers with those computed by Charpinet et al. (2011, Supplementary Information, Figure A.5; see also Pesnell 1985), allows us to exclude low inclinations and suggests an inclination of the rotation axis of $(65^{+10}_{-20})^{\circ}$.

3.3 Asteroseismic analysis

In order to obtain more insight about evolutionary status and interior of TIC 137608661, we calculated evolutionary models using the `MESA` code (Modules for Experiments in Stellar Astrophysics; Paxton et al. 2011, 2013, 2015, 2018, 2019), version 11701. The models were calculated for progenitors with initial masses, $M_{\rm i}$, in the range of $1.0 - 1.8\,M_{\odot}$, with a step of $0.01\,M_{\odot}$, and metallicities, Z, in the range of $0.005 - 0.035$, with a step of 0.005. The initial helium abundance was determined by the linear enrichment law, $\Delta Y/\Delta Z = 1.5$. The protosolar helium abundance, $Y_{\odot,\,\rm protosolar} = 0.2703$, and the mixture of metals were adopted from Asplund et al. (2009). The progenitors were evolved to the tip of the red giant branch where, before the helium ignition, most of the hydrogen has been removed leaving only a residual hydrogen envelope on top of the helium core. The considered envelope masses, $\mathrm{M_{env}}$, are in the range of $0.0001 - 0.0030\,M_{\odot}$, with a step of $0.0001\,M_{\odot}$. The models were then relaxed to an equilibrium state and evolved until the depletion of helium in the core. In all calculations we used the novel convective premixing scheme in order to ensure proper growth of the convective core during the course of evolution (Paxton et al. 2019). The thorough

Table 2. Orbital and pulsation frequencies.
(Errors in brackets are relative to the last digits, e.g. 38.526250 (11) means 38.526250±0.000011).

ID	F (μHz)	P (s)	A (ppt)	S/N	n[1]	*l*	m
f$_{\rm orb}$	38.526250 (11)	25956.3283 (72)	28.774 (17)				
2*f$_{\rm orb}$	77.052472 (65)	12978.169 (11)	4.738 (17)				
3*f$_{\rm orb}$	115.57770 (73)	8652.188 (55)	0.420 (17)				
4*f$_{\rm orb}$	154.1055 (12)	6489.062 (50)	0.261 (17)				
f1	93.0623 (10)	10745.49 (12)	0.297 (17)	11.0			
f2	93.15969 (99)	10734.26 (11)	0.311 (17)	11.6			
f3	109.3401 (21)	9145.78 (18)	0.144 (17)	5.4			
(f4	114.0211 (25)	8770.31 (19)	0.123 (17)	4.7)			
f5	125.1936 (19)	7987.63 (12)	0.162 (17)	6.2			
f6	148.63137 (40)	6728.055 (18)	0.764 (17)	30.1	26	1?	+1?
f6b[2]	148.6551 (12)	6726.982 (56)	0.249 (17)	9.8			
f7	155.6834 (17)	6423.292 (71)	0.179 (17)	7.1	25	1	0?
f8	156.9764 (23)	6370.385 (92)	0.136 (17)	5.4	25	1	+1?
f9	178.03636 (49)	5616.830 (16)	0.622 (17)	25.3	22	1?	+1?
f10	183.2003 (17)	5458.506 (50)	0.183 (17)	7.5	21	1	-1
f11	185.69940 (43)	5385.047 (13)	0.710 (17)	29.1	21	1	+1
f12	188.3160 (20)	5310.222 (57)	0.152 (17)	6.3			
f13	189.5612 (22)	5275.343 (62)	0.137 (17)	5.6			
f14	192.6449 (11)	5190.898 (31)	0.270 (17)	11.2	20	1	-1
f15	193.9138 (14)	5156.930 (37)	0.223 (17)	9.2	20	1	0
f16	195.1421 (19)	5124.472 (50)	0.162 (17)	6.7	20	1	+1
f17	203.00214 (44)	4926.056 (11)	0.693 (17)	29.0	19	1	-1?
f18	204.2614 (12)	4895.688 (29)	0.257 (17)	10.8	19	1	0?
f19	227.0400 (17)	4404.510 (32)	0.185 (17)	8.0		2?	
(f20	227.2388 (27)	4400.657 (53)	0.113 (17)	4.9)			
f21	230.30385 (78)	4342.090 (15)	0.392 (17)	16.9	17	1	+1?
(f22	252.9085 (30)	3953.999 (46)	0.104 (17)	4.6)			
f23	256.6026 (12)	3897.077 (18)	0.265 (17)	11.8		2?	
f24	260.61413 (52)	3837.0905 (77)	0.591 (17)	26.5	15	1	-1
f25	261.2016 (21)	3828.461 (30)	0.150 (17)	6.7		2?	
f26	261.86840 (70)	3818.712 (10)	0.440 (17)	19.8	15	1	0
(f27	263.1036 (29)	3800.785 (42)	0.105 (17)	4.7	15	1	+1)
f28	276.5385 (22)	3616.134 (28)	0.142 (17)	6.5		2	
f29	278.6794 (14)	3588.353 (18)	0.221 (17)	10.1		2	
f30	280.75348 (51)	3561.8436 (65)	0.601 (17)	27.6	14	1	-1
f31	282.00815 (58)	3545.9968 (73)	0.530 (17)	24.4	14	1	0
f32	283.23899 (57)	3530.5874 (71)	0.540 (17)	24.9	14	1	+1
f33	288.68769 (65)	3463.9510 (79)	0.470 (17)	21.8		2?	
f33b[3]	288.7149 (25)	3463.624 (30)	0.122 (17)	5.7			
f34	294.9645 (16)	3390.238 (19)	0.188 (17)	8.8		2	-1 or -2
f35	297.0378 (25)	3366.575 (28)	0.122 (17)	5.7		2	0 or -1
f36	301.3289 (29)	3318.632 (31)	0.108 (17)	5.1		2	+2 or +1
f37	304.84395 (40)	3280.3669 (43)	0.764 (17)	36.3	13	1	-1
f38	306.1024 (11)	3266.880 (11)	0.288 (17)	13.7	13	1	0
f39	307.33246 (65)	3253.8053 (69)	0.472 (17)	22.5	13	1	+1
(f40	320.8888 (31)	3116.344 (30)	0.099 (17)	4.8		2?)	
f41	332.78156 (70)	3004.9742 (63)	0.439 (17)	21.6	12	1	-1
f42	334.0450 (15)	2993.608 (13)	0.211 (17)	10.4	12	1	0
f43	335.27579 (52)	2982.6192 (46)	0.595 (17)	29.4	12	1	+1
(f44	365.4018 (32)	2736.714 (24)	0.095 (17)	4.9	11	1	0?)
f45	366.69996 (99)	2727.0251 (74)	0.311 (17)	16.1	11	1	+1?
f46	405.9003 (22)	2463.659 (13)	0.142 (17)	7.5	10	1	-1?
(f47	456.0976 (34)	2192.513 (16)	0.091 (17)	4.8	9	1	-1?)
f48	482.5889 (23)	2072.157 (10)	0.132 (17)	6.9			
f49	490.8909 (30)	2037.113 (13)	0.102 (17)	5.4			
f50	616.0114 (26)	1623.3466 (68)	0.119 (17)	6.3	7	1	+1?
f51	690.3358 (25)	1448.5704 (52)	0.124 (17)	6.5			

[1] Arbitrary offset. Assuming that the period spacing is constant, we consider n=1 for the shortest period.

[2] Residual (unresolved) peak after removing f6. See text for more details.

[3] Residual (unresolved) peak after removing f33. See text for more details.

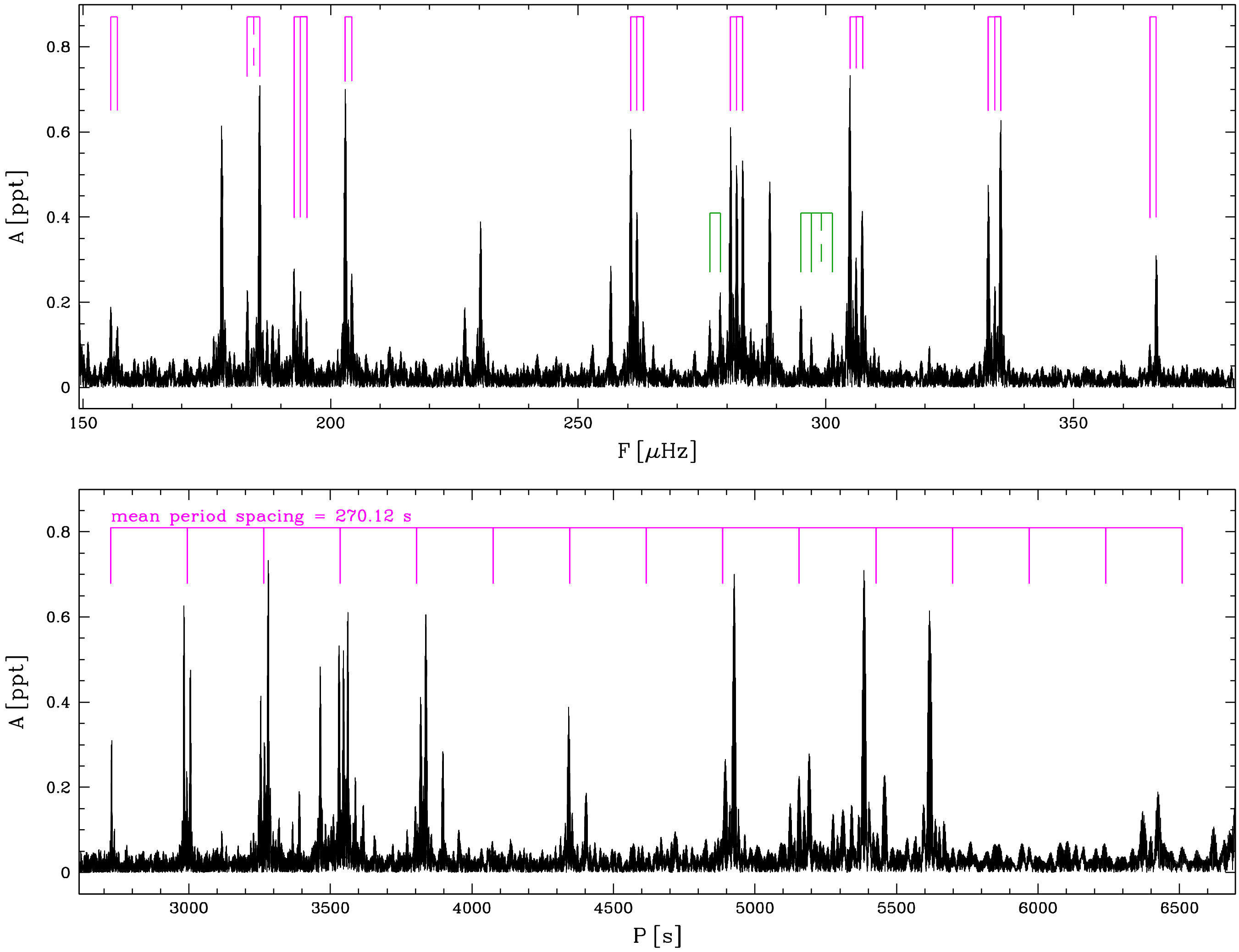

Figure 10. Frequency splitting (top) vs period spacing (bottom). Magenta refers to l=1 modes while green refers to l=2. Both panels represent exactly the same region of the spectrum.

description of the models is provided in Ostrowski et al. (2021). The adiabatic pulsation calculations were performed using the GYRE code, version 5.2 (Townsend & Teitler 2013; Townsend et al. 2018). The pulsation models were calculated for evolutionary models with central helium abundance, $Y_{\rm c}$, in the range of $0.9 - 0.1$, with a step of 0.05. The models with $Y_{\rm c} < 0.1$ were not considered due to the occurrence of the breathing pulses, which are unavoidable side effects of the convective premixing scheme (Ostrowski et al. 2021).

The grid of evolutionary models was used to find the models that represent TIC 137608661. No spectroscopic constraints were used in the process and we have chosen to fit only the five pulsation periods corresponding to the m=0 dipole modes identified via multiplet structures (f15, f26, f31, f38 and f42 in Table 2). We used a goodness-of-fit function, which calculates the difference between observed and theoretical periods

$$S^2 = \frac{1}{N_{\rm o}} \sum_{i=1}^{N_{\rm o}} \left(P_{\rm o}^i - P_{\rm c}^i \right)^2 , \qquad (1)$$

where $P_{\rm o}$ is an observed period, $P_{\rm c}$ is a calculated period, and $N_{\rm o}$ is the number of periods used (5 in this case). The minimum of the S^2 function indicates the best fit.

Considering only the six best solutions with S^2 up to about 150% of the minimum S^2, these best models clearly indicate that the progenitor of TIC 137608661 is a star with a metallicity close to solar, $Z = 0.01 - 0.015$, with a mass $M_{\rm i} = 1.1 - 1.2\,M_{\odot}$. The estimated age of the star is $5.4 - 7.3$ Gyr. The envelope mass of the star is constrained in the narrow range $M_{\rm env} = 0.0006 - 0.0009\,M_{\odot}$. As shown in Figure 14, the best solutions are located close to the spectroscopic determination of $T_{\rm eff}$ and $\log g$. Such spectroscopic values suggest a rather evolved EHB model, which is supported by the low central helium abundance of the best models, $Y_{\rm c} = 0.3 - 0.1$.

Table 3. SdB rotation (from asteroseismology) vs orbital periods.

Name*	$P_{\rm orb}$ (d)	$P_{\rm rot}$ (d) g-modes	$P_{\rm rot}$ (d) p-modes	Comments	Ref.
• sdB+dM binaries					
NY Vir (PG 1336-018)	0.10083		0.10083	rigid rot. down to 0.55 $R_\star$	(1)
TYC1 4544-2658-1 (TIC 137608661)	0.300	4.6			(2)
PHL 457 (EPIC 246023959)	0.31289	4.6	2.5 ?		(3)
V1405 Ori (EPIC 246683636)	0.39802	4.2 ?	0.555		(4)
B4 in NGC 6791 (KIC 2438324)	0.3985	9.63			(5,6)
KIC 11179657	0.394	7.4			(7,6)
KIC 2991403	0.443	10.3			(7,6)
EQ Psc (EPIC 246387816)	0.80083	9.4			(3)
• sdB+WD binaries					
HD 265435 (TIC 68495594)	0.0688185		0.069		(8)
KL UMa (Feige 48)	0.34361		0.38	rigid rotation	(9,10)
PG 1142-037 (EPIC 201206621)	0.5411	>45.			(11)
KIC 7664467	1.5590	35.1			(12)
EPIC 211696659	3.16	>28.			(13)
KIC 10553698	3.39	41.			(14)
KIC 11558725	10.05	$\sim$45.	$\sim$40.	$\sim$44 d rigid rotation	(15,16)
FBS 1903+432 (KIC 7668647)	14.17	46-48	49-52 ?	close to rigid rotation	(17)
• sdB+FGK wide binaries					
PG 0048+091 (EPIC 220614972)	?	13.9 ?	4.4	sdB+F	(18)
EPIC 211823779	?		11.5 ?	sdB+F1V	(13)
PG 1315-123 (EPIC 212508753)	?	15.8	16.2	sdB+F	(18)
EGGR 266 (EPIC 211938328)	635		21.5 ?	sdB+F6V	(13)
• single sdBs					
EPIC 211779126			$\sim$16	core rotation likely slower	(19)
UY Sex (EPIC 248411044)			24.6		(4)
KIC 10139564		$\sim$26	$\sim$26	rigid rotation	(20,21)
KY UMa (PG 1219+534)			34.9	rigid rot. down to 0.6 $R_\star$	(22)
KPD 1943+4058 (KIC 5807616)		39.2			(23)
KIC 2697388		$\sim$42	$\sim$53	close to rigid rotation	(24,25)
KIC 3527751		42.6	15.3 ??		(26,27)
EPIC 203948264		$\geq$45.9			(28)
TIC 33834484		64			(29)
EPIC 212707862		$\sim$80			(30)
KIC 10670103		88			(31)
KIC 1718290		$\sim$100		BHB star !	(32)
KIC 10001893		289			(33)

* Kepler/K2/TESS id are used as 1st or 2nd name when the results are based on Kepler/K2/TESS data.
(1) Charpinet et al. 2008; (2) this paper; (3) Baran et al. 2019; (4) Reed et al. 2020; (5) Pablo et al. 2011; (6) Baran & Winans 2012; (7) Pablo et al. 2012; (8) Pelisoli et al. 2021; (9) orbital period from TESS data preliminary analysis; (10) Van Grootel et al. 2008; (11) Reed et al. 2016; (12) Baran et al. 2016; (13) Reed et al. 2018b; (14) Østensen et al. 2014b; (15) Telting et al. 2012; (16) Kern et al. 2018; (17) Telting et al. 2014; (18) Reed et al. 2019; (19) Baran et al. 2017; (20) Baran et al. 2012; (21) Zong et al. 2016; (22) Van Grootel et al. 2018; (23) Charpinet et al. 2011 (SI); (24) Baran 2012; (25) Kern et al. 2017; (26) Foster et al. 2015; (27) Zong et al. 2018; (28) Ketzer et al. 2017; (29) Uzundag et al. in prep.; (30) Bachulski et al. 2016; (31) Reed et al. 2014; (32) Østensen et al. 2012; (33) Charpinet et al. 2018.

4 TIC 137608661 IN CONTEXT: SYNCHRONIZED VS NON-SYNCHRONIZED SDBS IN SHORT-PERIOD BINARIES

With an orbital period of 7.21 hours and an sdB rotation period of 4.6 days, TIC 137608661 is relatively far from synchronization. However, among the handful of sdB+dM binaries for which the sdB rotation was measured through asteroseismology, it is the non-synchronized system with both the shortest orbital period and the shortest sdB rotation period. Only PHL 457, with basically the same sdB rotation period and a slightly longer orbital period of 7.51 hours (Baran et al. 2019), ranks at the same level in the synchronization process. Table 3 shows the list of sdB/sdO stars for

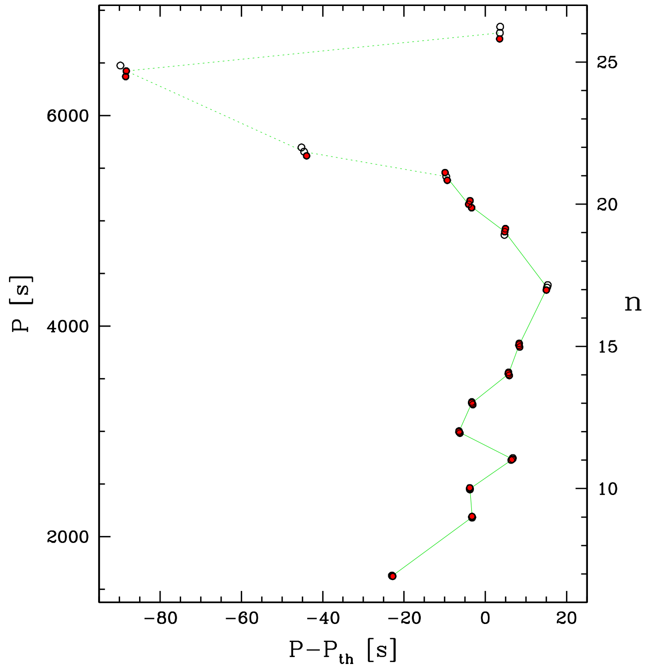

Figure 11. Échelle diagramme of the dipole modes showing the residuals between observed periods and theoretical periods computed assuming a constant period spacing of 270.116 s. The open dots are the missing components of the rotational triplets.

which the rotation period was measured from g- or p-mode frequency splitting.

A few stars are not reported Table 3: **KIC 2991276** since it is not clear whether this star is single or in a binary system. The short rotation period (6.3 d) measured from p-modes (Østensen et al. 2014a) suggests the presence of a companion and the low amplitude of the m=−1,+1 modes belonging to the triplets near 7560 and 8200 μHz suggest a low inclination $i \lesssim 15°$. A low inclination, together with KIC 2991276's faintness (17th-mag), means that it is not easy to verify the presence of a companion for this star. No rotational splitting was detected in **HD 4539/EPIC 220641886** and **KIC 8302197** (Silvotti et al. 2019; Baran et al. 2015a), suggesting long rotation periods (too long respect to the observing run) and/or a low inclination. With an orbital period of only 2.3 hours, the sdB+WD binary **KPD 1930+2752**, that shows also ellipsoidal variations, is likely synchronized. However, a clear detection of rotational splitting is missing (Billéres et al. 2000; Reed et al. 2011).

Focusing on short-period binaries (both sdB+dM and sdB+WD systems), Figure 15 includes also some systems for which the sdB rotation period is inferred from the rotational velocity measured through spectral line broadening: $P_{rot}=2\pi R \sin i/(v \sin i)$. This technique is more efficient at very short rotation periods, when the slow-rotation approximation normally used for the rotational splitting may no longer be valid. This might be the reason why no frequency multiplets were found in the amplitude spectrum of **2M 1938+4603**, an sdB+dM binary with an orbital period of 3.02 hours (Baran et al. 2015b, and references therein). We see from Figure 15 that synchronization occurs for orbital periods shorter than ∼0.3 days (first group of stars), while at orbital periods longer than ∼1 day (second group) the rotation periods are close to the typical values of single stars, of a few tens of days. Between these two groups, a third group is formed by the stars that are approaching synchronization. It is important to note that different methods were used to measure P_{rot} in these three groups and these methods sample different regions of the star: internal layers with the g-mode frequency splitting used in group 2 and 3, external layers with the spectral-line broadening or p-mode frequency splitting used in group 1. Indeed, a few systems in Table 3, for which the sdB rotation was measured at different depths, suggest that differential rotation might be quite common in these stars. And this can partially explain why the jump between group 2 and 3 and group 1 that we see in Figure 15 is so steep.

Figure 15 suggests a few further comments: in group 1 the three systems that have a brown dwarf (BD) companion (represented with red empty diamonds) are not fully synchronized, differently from the other sdB+dM systems with similar orbital periods. Although we do not know their evolutionary phase, this effect is probably related to their longer synchronization time which is inversely proportional to the companion mass. At longer orbital periods, the two sdB/sdO+WD systems **PG 2345+318** and **EVR-CB-004** (blue circles in Figure 15), with almost identical orbital periods of 0.24 and 0.25 d respectively, have significantly different rotation periods. But EVR-CB-004 hosts a peculiar object with a radius of 0.63 $R_\odot$ that can be either an inflated sdO star or, more likely, a post-blue horizontal branch star (Ratzloff et al. 2020a). With such a radius, it is not surprising that the star was most affected by the tidal effects from its WD companion. PG 2345+318, on the other hand, is a key object in a transition region between non-synchronized and synchronized systems. We know that it must have an inclination close to 90° because Green et al. (2004) saw a primary (and may be a secondary) eclipse in the light curve. Thus, from $\log g$=5.70 (Geier et al. 2010, and references therein) and assuming i=90° and M=0.47$M_\odot$, we obtain $P_{rot}\simeq$0.63 d. Another interesting system, **PG 1232-136**, with an orbital period of 0.363 d and a very low rotational velocity $v_{rot} \sin i$<5 km/s (Geier et al. 2010, and references therein), is not represented in Figure 15 since the unknown inclination leaves two different possibilities open: a) the system is not synchronized and the companion is likely a white dwarf; b) the system is synchronized, the inclination must be very low (i<14°), and the companion is a black hole candidate. From a preliminary analysis of the *TESS* data, the light curve of PG 1232-136 shows a weak (730 ppm) orbital modulation at exactly the orbital period.

5 SUMMARY

TIC 033834484 is a new sdB+dM binary with an orbital period of 7.21 hours. The *TESS* light curve shows the typical orbital modulation produced by the heating of the secondary star and shows also a rich spectrum of g-mode pulsations from the primary.

The atmospheric parameters of the sdB star are well compatible with the g-mode instability strip. From 13 low-resolution spectra collected with ALFOSC@NOT we obtain $T_{\rm eff}$=27300±200 K, $\log g$=5.39±0.04, $\log(N_{He}/N_H)$=−

2.95±0.05 or $T_{\rm eff}$=27960±50 K, log g=5.42±0.04, log($N_{\rm He}/N_{\rm H}$)=–2.89±0.05 from LTE or non-LTE models respectively. The chemical abundances from non-LTE models are typical for N, O, Ne and Fe, while the star is relatively poor in C and Mg and especially in Si (see e.g. Heber 2016, and references therein).

The amplitude spectrum is particularly simple to interpret as we see five well defined l=1 triplets of frequencies in which all the three m=–1,0,+1 components are clearly visible. A few more incomplete triplets are also present, that allow us to obtain a l=1 mean period spacing ΔP= 270.12 ± 1.19. The mean l=1 frequency splitting of 1.254 μHz corresponds to a very robust rotation period of about 4.6 days in the internal layers of the star. From the mean amplitude of the m=–1,+1 modes of the five complete triplets we can also constrain the inclination of the system and we obtain i=$(65^{+10}_{-20})^{\circ}$.

The spectroscopic measurements of $T_{\rm eff}$ and log g are in good agreement with the best values that we obtain from an asteroseismic analysis using the `MESA` code. Adiabatic pulsation computations applied to the best evolutionary models and compared with the observed pulsation periods, suggest that the progenitor of TIC 033834484's primary was a star with an initial mass of 1.1–1.2 $M_{\odot}$, with a solar metallicity. They suggest also that the sdB star has an envelope mass of 0.0006–0.0009 $M_{\odot}$ and is rather evolved, with a central helium abundance of 10–30%. Finally, they indicate that the total age of the system is 5.4–7.3 Gyr.

Since the SED of TIC 033834484 does not show any contribution from the companion, we can infer that its effective temperature mut be lower than about 4000 K. Moreover, from both the SED and the asteroseismic analysis (section 2.3 and 3.3), we can assume that the sdB mass is between 0.42 and 0.47 $M_{\odot}$. Then, from $P_{\rm orb}$=0.300 d and K≃42 km/s, we obtain that the companion mass should be M_c sin$i$=87–94 $M_{\rm Jup}$, not far from the hydrogen burning limit. Which means a mass of ∼96–104 $M_{\rm Jup}$ if the inclination is indeed 65°.

The measurement of the rotation period of TIC 033834484 is important because only in a handful of sdB stars the rotational splitting is so well defined, leading to a robust determination of the rotation period. It is particularly interesting because TIC 033834484 falls in a critical and poorly populated region of the $P_{\rm orb}$-$P_{\rm rot}$ plane (Figure 15), in which the star is gaining angular momentum without having already reached the full synchronization with the orbital period.

To measure the sdB rotation in sdB+dM/sdB+WD short-period binaries is of considerable importance for guiding theoretical studies on tides and tidal synchronization time-scales. As pointed out by Preece et al. (2018), sdB synchronization time-scales seem to be longer than the sdB lifetime and, in particular, the synchronization of NY Vir remains not explained by current models, even when we consider a larger convective core (Preece et al. 2019). Potential explanations given by these authors for the synchronization of NY Vir are a partial synchronization of at least the outer layers of the star already during the common envelope phase, or higher convective mixing velocities respect to those obtained with the mixing length theory.

ACKNOWLEDGEMENTS

This paper is based on photometric data collected by the *TESS* space telescope and spectroscopic data collected with the 2.6 m Nordic Optical Telescope (NOT), operated jointly by Denmark, Finland, Iceland, Norway, and Sweden. Funding for the *TESS* mission is provided by the NASA Explorer Program. Funding for the *TESS* Asteroseismic Science Operations Centre is provided by the Danish National Research Foundation (Grant agreement n. DNRF106), ESA PRODEX (PEA 4000119301) and Stellar Astrophysics Centre (SAC) at Aarhus University. We thank the *TESS* team and the TASC/TASOC team for their support to the present work and in particular we thank Stéphane Charpinet for organising and coordinating the TASC Working Group 8 on Evolved Compact Stars. RS acknowledges financial support from the INAF project on "Stellar evolution and asteroseismology in the context of the PLATO space mission" (PI S. Cassisi). Asteroseismic analysis calculations have been carried out using resources provided by Wroclaw Centre for Networking and Supercomputing (http://wcss.pl), grant No. 265. Financial support from the National Science Centre under projects No. UMO-2017/26/E/ST9/00703 and UMO-2017/25/B/ST9/02218 is acknowledged.

DATA AVAILABILITY

The *TESS* data underlying this article is publicly available, the spectroscopic data may be requested to the authors.

REFERENCES

Aerts C., Christensen-Dalsgaard J., Kurtz D. W., 2010, Asteroseismology. Astronomy and Astrophysics Library, Springer Science+Business Media B.V.

Asplund M., Grevesse N., Sauval A. J., Scott P., 2009, ARA&A, 47, 481

Bachulski S., Baran A. S., Jeffery C. S., Østensen R. H., Reed M. D., Telting J. H., Kuutma T., 2016, Acta Astron., 66, 455

Baran A. S., 2012, Acta Astron., 62, 179

Baran A. S., Koen C., 2021, arXiv e-prints, p. arXiv:2106.09718

Baran A. S., Winans A., 2012, Acta Astron., 62, 343

Baran A. S., et al., 2012, MNRAS, 424, 2686

Baran A. S., Telting J. H., Németh P., Bachulski S., Krzesiński J., 2015a, A&A, 573, A52

Baran A. S., Zola S., Blokesz A., Østensen R. H., Silvotti R., 2015b, A&A, 577, A146

Baran A. S., Telting J. H., Németh P., Østensen R. H., Reed M. D., Kiaeerad F., 2016, A&A, 585, A66

Baran A. S., Reed M. D., Østensen R. H., Telting J. H., Jeffery C. S., 2017, A&A, 597, A95

Baran A. S., et al., 2018, MNRAS, 481, 2721

Baran A. S., Telting J. H., Jeffery C. S., Østensen R. H., Vos J., Reed M. D., Vučković M., 2019, MNRAS, 489, 1556

Billéres M., Fontaine G., Brassard P., Charpinet S., Liebert J., Saffer R. A., 2000, ApJ, 530, 441

Budaj J., 2011, AJ, 141, 59

Charpinet S., Van Grootel V., Reese D., Fontaine G., Green E. M., Brassard P., Chayer P., 2008, A&A, 489, 377

Charpinet S., et al., 2011, Nature, 480, 496

Charpinet S., Giammichele N., Zong W., Van Grootel V., Brassard P., Fontaine G., 2018, Open Astronomy, 27, 112

Clausen D., Wade R. A., Kopparapu R. K., O'Shaughnessy R., 2012, ApJ, 746, 186

Deca J., et al., 2012, MNRAS, 421, 2798
Drechsel H., et al., 2001, A&A, 379, 893
Esmer E. M., Baştürk Ö., Hinse T. C., Selam S. O., Correia A. C. M., 2021, A&A, 648, A85
Foster H. M., Reed M. D., Telting J. H., Østensen R. H., Baran A. S., 2015, ApJ, 805, 94
Geier S., Heber U., Podsiadlowski P., Edelmann H., Napiwotzki R., Kupfer T., Müller S., 2010, A&A, 519, A25
Green E. M., et al., 2004, Ap&SS, 291, 267
Han Z., Podsiadlowski P., Maxted P. F. L., Marsh T. R., Ivanova N., 2002, MNRAS, 336, 449
Han Z., Podsiadlowski P., Maxted P. F. L., Marsh T. R., 2003, MNRAS, 341, 669
Heber U., 2016, PASP, 128, 966
Heber U., Reid I. N., Werner K., 2000, A&A, 363, 198
Hubeny I., Lanz T., 2017, arXiv e-prints, p. arXiv:1706.01859
Kepler S. O., 1993, Baltic Astronomy, 2, 515
Kern J. W., Reed M. D., Baran A. S., Østensen R. H., Telting J. H., 2017, MNRAS, 465, 1057
Kern J. W., Reed M. D., Baran A. S., Telting J. H., Østensen R. H., 2018, MNRAS, 474, 4709
Ketzer L., Reed M. D., Baran A. S., Németh P., Telting J. H., Østensen R. H., Jeffery C. S., 2017, MNRAS, 467, 461
Kupfer T., et al., 2017, ApJ, 835, 131
Kupfer T., et al., 2020a, ApJ, 891, 45
Kupfer T., et al., 2020b, ApJ, 898, L25
Lanz T., Hubeny I., 2007, ApJS, 169, 83
Ledoux P., 1951, ApJ, 114, 373
Maxted P. F. L., Marsh T. R., Heber U., Morales-Rueda L., North R. C., Lawson W. A., 2002, MNRAS, 333, 231
Morrissey P., et al., 2007, ApJS, 173, 682
Németh P., Kawka A., Vennes S., 2012, MNRAS, 427, 2180
Østensen R. H., et al., 2010, A&A, 513, A6
Østensen R. H., et al., 2012, ApJ, 753, L17
Østensen R. H., Reed M. D., Baran A. S., Telting J. H., 2014a, A&A, 564, L14
Østensen R. H., Telting J. H., Reed M. D., Baran A. S., Nemeth P., Kiaeerad F., 2014b, A&A, 569, A15
Ostrowski J., Baran A. S., Sanjayan S., Sahoo S. K., 2021, MNRAS, 503, 4646
Pablo H., Kawaler S. D., Green E. M., 2011, ApJ, 740, L47
Pablo H., et al., 2012, MNRAS, 422, 1343
Paxton B., Bildsten L., Dotter A., Herwig F., Lesaffre P., Timmes F., 2011, ApJS, 192, 3
Paxton B., et al., 2013, ApJS, 208, 4
Paxton B., et al., 2015, ApJS, 220, 15
Paxton B., et al., 2018, ApJS, 234, 34
Paxton B., et al., 2019, ApJS, 243, 10
Pelisoli I., Vos J., Geier S., Schaffenroth V., Baran A. S., 2020, arXiv e-prints, p. arXiv:2008.07522
Pelisoli I., et al., 2021, arXiv e-prints, p. arXiv:2107.09074
Pesnell W. D., 1985, ApJ, 292, 238
Preece H. P., Tout C. A., Jeffery C. S., 2018, MNRAS, 481, 715
Preece H. P., Tout C. A., Jeffery C. S., 2019, MNRAS, 485, 2889
Ratzloff J. K., et al., 2019, ApJ, 883, 51
Ratzloff J. K., et al., 2020a, ApJ, 890, 126
Ratzloff J. K., et al., 2020b, ApJ, 902, 92
Reed M. D., et al., 2011, MNRAS, 412, 371
Reed M. D., Foster H., Telting J. H., Østensen R. H., Farris L. H., Oreiro R., Baran A. S., 2014, MNRAS, 440, 3809
Reed M. D., et al., 2016, MNRAS, 458, 1417
Reed M. D., et al., 2018a, Open Astronomy, 27, 157
Reed M. D., et al., 2018b, MNRAS, 474, 5186
Reed M. D., et al., 2019, MNRAS, 483, 2282
Reed M. D., Yeager M., Vos J., Telting J. H., Østensen R. H., Slayton A., Baran A. S., Jeffery C. S., 2020, MNRAS, 492, 5202
Schaffenroth V., Geier S., Heber U., Kupfer T., Ziegerer E., Heuser C., Classen L., Cordes O., 2014, A&A, 564, A98
Schaffenroth V., Barlow B. N., Drechsel H., Dunlap B. H., 2015, A&A, 576, A123
Schaffenroth V., et al., 2021, MNRAS, 501, 3847
Schlafly E. F., Finkbeiner D. P., 2011, ApJ, 737, 103
Silvotti R., et al., 2019, MNRAS, 489, 4791
Silvotti R., et al., 2021, MNRAS, 500, 2461
Telting J. H., et al., 2012, A&A, 544, A1
Telting J. H., et al., 2014, A&A, 570, A129
Townsend R. H. D., Teitler S. A., 2013, MNRAS, 435, 3406
Townsend R. H. D., Goldstein J., Zweibel E. G., 2018, MNRAS, 475, 879
Unno W., Osaki Y., Ando H., Saio H., Shibahashi H., 1989, Nonradial oscillations of stars. Tokyo: University of Tokyo Press, 2nd ed.
Uzundag M., Baran A. S., Østensen R. H., Reed M. D., Telting J. H., Quick B. K., 2017, MNRAS, 472, 700
Van Grootel V., Charpinet S., Fontaine G., Brassard P., 2008, A&A, 483, 875
Van Grootel V., Péters M.-J., Green E. M., Charpinet S., Brassard P., Fontaine G., 2018, Open Astronomy, 27, 44
Vennes S., Kawka A., O'Toole S. J., Németh P., Burton D., 2012, ApJ, 759, L25
Vučković M., Østensen R. H., Németh P., Bloemen S., Pápics P. I., 2016, A&A, 586, A146
Wolz M., et al., 2018, Open Astronomy, 27, 80
Zong W., Charpinet S., Vauclair G., 2016, A&A, 594, A46
Zong W., Charpinet S., Fu J.-N., Vauclair G., Niu J.-S., Su J., 2018, ApJ, 853, 98

This paper has been typeset from a TEX/LATEX file prepared by the author.

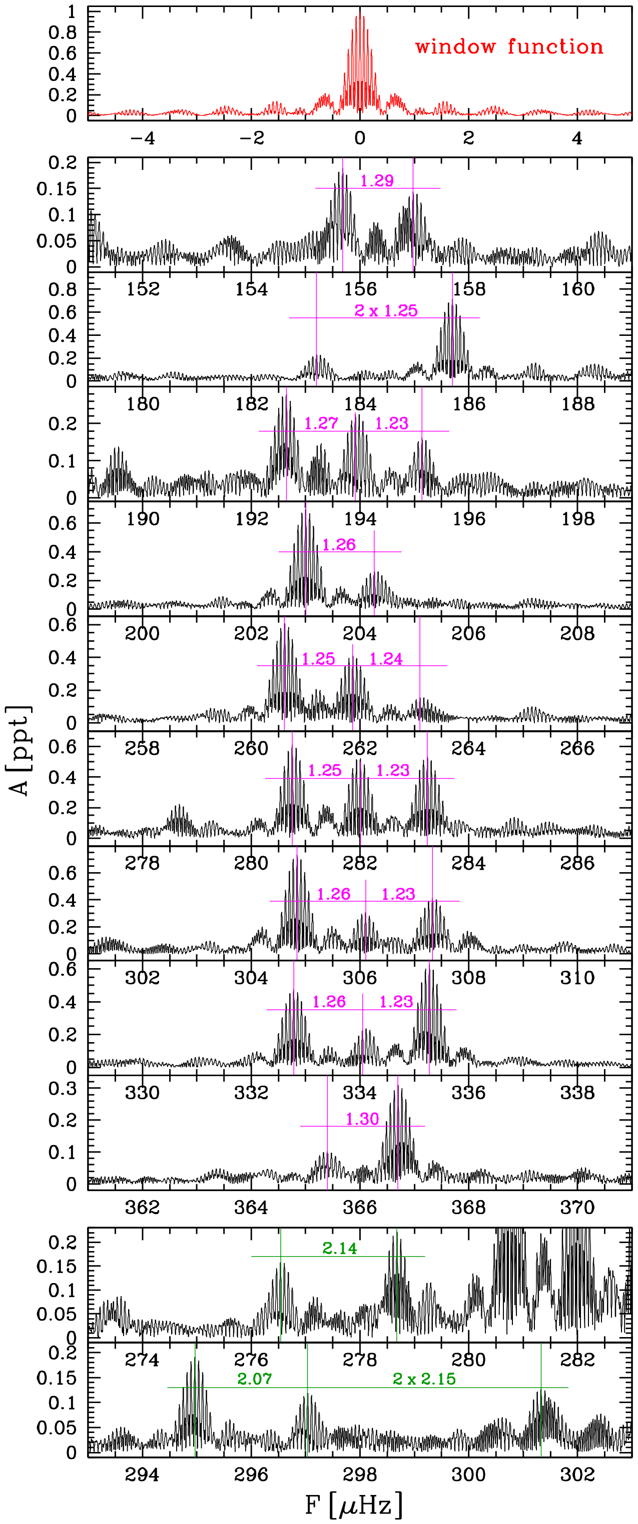

Figure 12. Frequency splitting in detail: the nine complete or incomplete l=1 triplets and the two incomplete l=2 quintuplets.

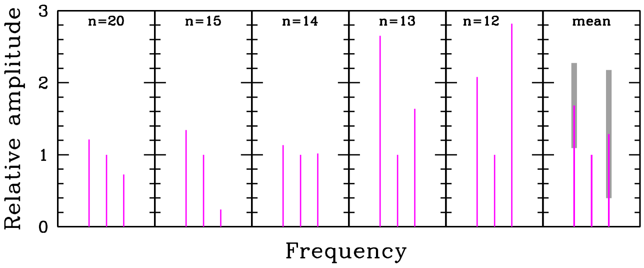

Figure 13. Relative amplitudes of the components of the five l=1 triplets. The amplitude of the central component of each triplet is normalized to 1 before computing the mean amplitudes, which are shown in the rightmost panel. The error bars (in grey) are the standard deviations around the mean amplitudes.

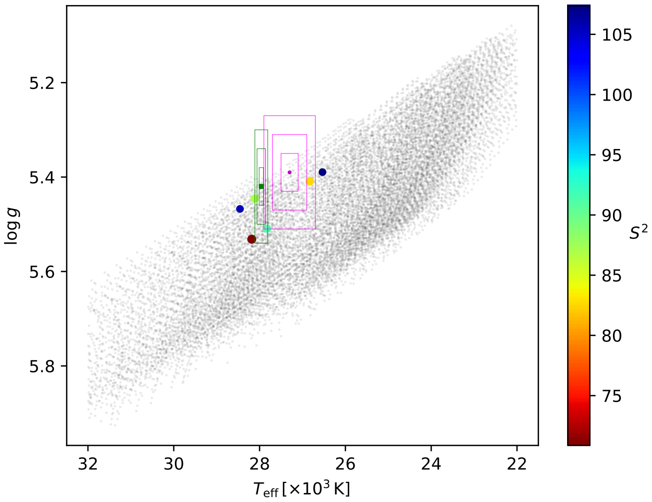

Figure 14. Asteroseismic determination of $T_{\rm eff}$ and $\log g$. Color coded S^2 (as defined in equation 1) outlines the best models. Minimum S^2 is obtained for $T_{\rm eff}$=28180 K and $\log g$=5.53 (dark-red point). Magenta and dark-green small points/rectangles represent spectroscopic $T_{\rm eff}$ and $\log g$ with 1, 2 and 3 σ error boxes, from LTE and non-LTE models respectively.

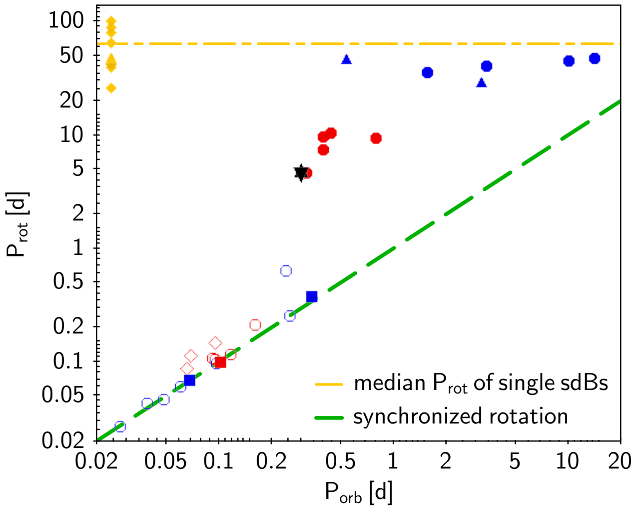

Figure 15. SdB rotation period vs orbital period. Red symbols: sdB+dM systems with sdB rotation period obtained from g-mode or p-mode frequency splitting (filled circles and filled square respectively) or from spectral line broadening (empty circles or empty diamonds, the latter indicating a brown dwarf companion). Black star: TIC 033834484. Blue symbols: sdB+WD systems with sdB rotation period obtained from g-mode frequency splitting (filled circles or filled triangles that indicate a lower limit) or p-mode frequency splitting (filled squares) or from spectral line broadening (empty circles). Yellow symbols: single sdB stars with rotation period obtained from g-mode frequency splitting (triangle indicating a lower limit). The seven red empty symbols correspond to the following HW Virginis (eclipsing sdB+dM/BD) systems: from left to right V 2008-1753 (Schaffenroth et al. 2015, 2021), SDSS J162256.66+473051.1 (Schaffenroth et al. 2014), PTF1 J011339.09+225739.1 (Wolz et al. 2018), HS 0705+6700 (Drechsel et al. 2001), SDSS J082053.53+000843.4 (Schaffenroth et al. 2021), HW Vir (Geier et al. 2010; Baran et al. 2018; Esmer et al. 2021), EPIC 216747137 (Silvotti et al. 2021). The seven blue empty circles correspond to the following non-eclipsing (or partially eclipsing) sdB+WD binaries: from left to right ZTF J2130+4420 (Kupfer et al. 2020a), ZTF J2055+4651 (Kupfer et al. 2020b), CD-30°11223 (Vennes et al. 2012), PTF1 J0823+0819 (Kupfer et al. 2017), EVR-CB-001 (Ratzloff et al. 2019), PG 2345+318 (Geier et al. 2010; Green et al. 2004), EVR-CB-004 (Ratzloff et al. 2020b).